Dalton Transactions

PAPER

View Article Online
View Journal | View Issue

Cite this: *Dalton Trans.*, 2025, **54**, 15816

Indications of ferroelectric behaviour near room temperature in the organic–inorganic hybrid Q_2CuBr_4

Agnieszka Ciżman, *[a] Dorota A. Kowalska, [b] Paweł Szarek, [c] Wojciech Medycki, [d] Natalia A. Wójcik, [e] Marek Gusowski, [a] Monika Trzebiatowska, [b] Adam Bartosiewicz, [a] Liudmyla Filevska, [a] Piotr Staniorowski [f] and Ewelina Jach *[a]

Received 16th July 2025,
Accepted 25th September 2025

DOI: 10.1039/d5dt01668a

rsc.li/dalton

A quinuclidinium-based copper bromide molecular ferroelectric, exhibiting a polarization of P_s = 0.52 μC cm^{-2} at zero electric field, has been successfully synthesized. This compound undergoes an order–disorder phase transition at T_c = 295 K, associated with thermally induced rotational motion of the quinuclidinium cations. This transition results in pronounced changes in both the dielectric constant and thermal properties. The contributions of the organic and inorganic components, as well as their interactions, to the observed electrical and thermal behaviors are discussed using both experimental data and theoretical analysis.

1. Introduction

Among functional materials, hybrid organic–inorganic compounds (HOICs) occupy a significant position due to their unique physicochemical properties, resulting from the combination of organic and inorganic components.[1,2] The complexes of these spherical organic amines with metal halides have attracted considerable interest from researchers.[3–7] The literature highlights the catalytic properties of quinuclidines and their derivatives, particularly in hydrogen atom transfer reactions,[8] as well as their pharmacological applications.[9] However, the most intriguing properties of these compounds are associated with phase transitions. The switchable dielectric[3,6,10,11] and magnetic behaviors,[11–13] as well as thermochromic, photoelectric effects, and photoluminescence,[7,13] make them highly desirable for applications in optoelectronics, sensors, data storage systems, and switches.

Quinuclidines (1-azabicyclo[2.2.2]octane, denoted as Q) and DABCO (1,4-diazabicyclo[2.2.2]octane) act as organic cations that stabilize the inorganic frameworks of metal halides. For instance, hybrid copper halides synthesized by solvothermal method in ref. 7, in the form one-dimensional chains, are supported by organic cations (complexes [(Me)$_2$-DABCO]Cu_2I_4 and [H_2-DABCO]Cu_3Br_5) through varied interactions, mostly hydrogen bonding (HB).[14] When combined with hydrogen bond dynamics, this stabilization results in unique photoluminescence across a range from blue to red light.[7]

The ammonium cations exhibit rotational motions with temperature changes, which often initiate order–disorder phase transitions (PTs). In ref. 15, the X-ray structural analysis and DSC revealed that the rotational disordering of dabco molecules in [Ni^{2+}(acac)$_2$(abco)$_2$] compound by 60 degrees at approximately 225 K induces a change in local symmetry from trigonal to hexagonal. This reduction in crystal symmetry gives rise to new structural features and, consequently, new properties. The dynamics of organic cations, being a key driver of order–disorder phase transitions, leads to switchable dielectric permittivity and magnetic properties in quinuclidinium chlorides,[11] highlighting their potential for use in smart devices.

Additionally, the critical role of quinuclidine ring dynamics in [$(CH_3)_2CH$-$C_3H_{17}N$][$CoBr_4$] in the phase transition mechanism of the [$(CH_3)_2CH$-$C_3H_{17}N$]$^{2+}$ cation was confirmed.[3] The structural changes in hybrid quinuclidine-metal bromide compounds ($(C_7H_{14}N)_2MBr_4$ (M = Co, Mn, Cd) during phase transitions involve the dynamics of organic cations accompanied by the formation of new hydrogen bonds.[16] In fact, the hydro-

---

[a] Department of Experimental Physics, Wrocław University of Science and Technology, Wybrzeże Wyspiańskiego 27, 50-370 Wrocław, Poland. E-mail: agnieszka.cizman@pwr.edu.pl, ewelina.jach@pwr.edu.pl
[b] Institute of Low Temperature and Structure Research, Polish Academy of Sciences, Okólna 2, 50-422 Wrocław, Poland
[c] Navi-Chem®, Włodarzewska 83/120, Warsaw, Poland
[d] Institute of Molecular Physics, Polish Academy of Science, M. Smoluchowskiego 17, 60-179 Poznań, Poland
[e] Institute of Nanotechnology and Material Engineering, Gdansk University of Technology, Narutowicza 11/12, 80-233 Gdansk, Poland
[f] Institute of Experimental Physics, University of Wrocław, Pl. M. Borna 9, 50204 Wrocław, Poland

gen bond dynamics in HOICs emerges as another key factor influencing phase transitions and altering the dielectric and optical properties of these materials.[7,11,16] The past few years have seen the rational design of molecular quinuclidine-based novel functional dielectrics and ferroelectrics.[10,11,16–18] It has been shown, that molecules, like quinuclidine similar to DABCO, are excellent units for design of switchable dielectrics and ferroelectrics owing to their structural phase transitions.[7–11,17,18] The studies of the dielectric properties of quinuclidinium metal chlorides and bromides have shown a high repeatability and stability in switching between high- and low-dielectric states. The high-dielectric "ON" state, associated with dipolar reorientation, is observed above phase transition, while the low-dielectric "OFF" state, where reorientations are "frozen", occurs at temperatures below the phase transition point.[11,16] For example, in the previously studied material Q_2CuCl_4, which is a chloride analogue to the present crystal, the phase transition is present at 347 K on cooling, with a symmetry change from *Pnma* to $P2_1/c$, which is majorly the result of quinuclidine reorientation.[11] This behavior makes these materials promising for use in temperature sensors and dielectric switches. Despite the significant attention given to hybrid compounds with DABCO or quinuclidines, the properties of their complexes with metal bromides remain insufficiently explored, particularly in the context of their phase transitions and switchable properties.

In this study, we investigate a new hybrid organic–inorganic compound, $(C_7H_{14}N)_2CuBr_4$ (Q_2CuBr_4), featuring a copper bromide inorganic framework. Based on analogies with related systems, the material was expected to exhibit distinct phase transitions driven by both structural factors and quinuclidinium cation dynamics. To explore its thermal, structural, and electrical behavior, techniques such as DSC, X-ray diffraction, IR and Raman spectroscopy, ^1H NMR, and EPR were used. The aim is to characterize the phase transitions and assess the functional potential of Q_2CuBr_4, contributing to the broader understanding of structure–property relationships in HOICs.

2. Methods

Synthesis

Copper(II) bromide ($CuBr_2$, 98%, Thermo Scientific), quinuclidine (1-azabicyclo[2.2.2]octane, 98%, AmBeed), hydrobromic acid (HBr, 48% in water, Fluorochem), methanol (99.85%, Fisher), and acetonitrile (HPLC grade, Chempur) were used as received. Crystals of $(\text{quinuclidinium}\cdot HBr)_2CuBr_4$ were obtained using a 2 : 1 molar ratio of quinuclidine to $CuBr_2$. Quinuclidine (2 mmol, 222 mg) was dissolved in 30 mL of methanol/acetonitrile (1 : 1, v/v), which acted as both solvent and thermal buffer during salt formation. HBr (~2 mL) was added dropwise until the solution reached pH ≈ 1, forming the quinuclidinium hydrobromide salt *in situ*. Separately, $CuBr_2$ (1 mmol, 223 mg) was dissolved in 20 mL of the same solvent mixture with a few drops of HBr. The two solutions were combined under stirring, yielding a homogeneous transparent solution, which was left to evaporate slowly at room temperature. Dark green to black crystals of $(\text{quinuclidinium}\cdot HBr)_2CuBr_4$ formed over several days and were collected in 91% yield (based on $CuBr_2$) without further purification.

Thermal properties

Differential scanning calorimetry (DSC) measurements were conducted using a Mettler Toledo instrument. The tests were performed in aluminum crucibles under a nitrogen atmosphere. A dry powder sample of Q_2CuBr_4 (22.92 mg) was heated and cooled at a rate of 10 K min^{-1} within the temperature range of 280–330 K.

Structure determination

Single crystal diffraction measurements were conducted on a good-quality Q_2CuBr_4 crystal using an Oxford X'Calibur four-circle diffractometer with a graphite-monochromated Mo Kα (λ = 0.71073 Å) radiation source and a CCD Atlas detector. To maintain non-ambient temperatures, an Oxford Cryosystem 800 series cryocooler was utilised. Data collection and reduction were performed using the CrysAlis PRO[19] software. Empirical absorption correction were applied using spherical harmonics, implemented through the SCALE3ABSPACK scaling algorithm, alongside numerical absorption correction based on Gaussian integration over a multifaceted crystal model. Measurements at various temperature points were obtained from the same crystal sample. The crystallographic data summary is available from the Cambridge Crystallographic Data Centre, with deposition numbers CCDC 2417202 and 2417203.

The crystallographic software package SHELX-2014,[20,21] integrated into the Olex2[22] program, was employed for structure solution *via* direct methods and for refinement using full-matrix least-squares methods on F^2. Non-hydrogen atoms were refined anisotropically, with the exception of the carbon atoms in the disordered Q ion within disordered phase I. In both of presented Q_2CuBr_4 phases H-atom parameters were constrained. Details of the crystal data, along with experimental and refinement information, are summarized in Table 1.

To verify the phase purity of the bulk sample, powder X-ray diffraction (PXRD) data were collected. The PXRD measurements were conducted in reflection mode using a PANalytical X'Pert diffractometer equipped with a PIXcel solid-state linear detector and utilizing Cu Kα (λ = 1.5418 Å) radiation (Fig. S1).

Electrical investigation

Dielectric measurements were performed on pelletized samples of Q_2CuBr_4, prepared by pressing polycrystalline powder into discs. Silver conductive paste was applied to both flat surfaces to serve as electrodes. Temperature-dependent dielectric constants were measured using a Novocontrol Alpha Impedance Analyzer over the frequency range of 1 MHz to 1 Hz with an applied AC field of 1 V, in the temperature range 200–340 K. Temperature control was achieved using a nitrogen gas cryostat with a stability better than ±0.1 K.

Table 1 The diffraction experimental details

Phase	II (ordered)	I (disordered)
Crystal data		
Chemical formula	$2(C_7H_{14}N)\cdot CuBr_4$	
M_r	607.56	
Crystal system, space group	Monoclinic, *Pc* (no. 7)	Monoclinic, $P2_1/c$ (no. 14)
T (K)	100	300
a, *b*, *c* (Å)	9.450(2), 16.929(4), 12.435(3)	9.552(3), 17.154(5), 12.593(4)
β (°)	94.15(2)	93.34(3)
V (Å^3)	1984.1(8)	2059.9(11)
Z	4	
μ (mm^{-1})	9.15	8.82
Crystal size (mm)	0.29 × 0.23 × 0.17	
Data collection		
Refl. measured/unique/observed [$I > 2\sigma(I)$]	33 758/9302/8872	14 987/4829/3118
R_{int}	0.025	0.027
Refinement		
$R[F^2 > 2\sigma(F^2)]$, w$R(F^2)$, *S*	0.020, 0.040, 1.04	0.047, 0.108, 1.02
Data/parameters/restraints	9302/381/2	4829/191/2
$\Delta\rho_{max}$, $\Delta\rho_{min}$ (e Å^{-3})	0.41, −0.38	0.93, −0.69
Absolute structure	Refined as an inversion twin	—
Abs. struct. parameter	0.476(8)	—

Ferroelectric hysteresis loops were recorded using a Keithley 6517A High-Resistance Meter under a triangular electric field (10–2 Hz) with an amplitude of 2000 V cm^{-1}.

Nonlinear impedance measurements were performed in a nitrogen atmosphere over a frequency range of 10 Hz to 1000 Hz, using an U_{AC} of 3 V_{rms}, within a temperature range of 233 to 333 K. A higher bias of 3 V_{rms} was applied in order to enhance the visibility of nonlinear effects that are already present at 1 V_{rms}. To avoid electrode polarization, measurements were carried out only above 10 Hz, during both heating and cooling, with finer temperature steps near the ~300 K phase transition. The impedance components corresponding to higher harmonics were defined as the ratio of the fundamental voltage wave to the *n*-th harmonic current component: $Z_n^* = U_1^*/I_n^*$, where Z_n^* including the fundamental wave, generally depends on the amplitude of the fundamental voltage wave U_1^* applied to the sample. Consequently, the current density can be expressed as:

$$j' = \sigma'_{1h}E_0\cos(\omega t) + \sigma'_{2h}E_0\cos^2(2\omega t) + \sigma'_{3h}E_0\cos^3(3\omega t) + \ldots \tag{1}$$

The fundamental conductivity, σ'_{1h}, represents the base conductivity, while σ'_{2h}, σ'_{3h}, and higher-order terms correspond to the conductivity of the respective harmonic components while $E_0 = U_0/d \quad U_0\sqrt{2U_{AC}}$. The admittivity for harmonic components with $n \geq 2$ is determined using the relation:

$$\sigma_n^* = i2\pi f\varepsilon_0\varepsilon_n^* \tag{2}$$

The used Novocontrol system enables the separation of the fundamental (first harmonic) from higher harmonics (2nd and 3rd), ensuring that the detected nonlinear signal is genuine and not an artifact of the measurement.

NMR study

^{1}H NMR experiments were carried out using an ELLAB TEL-Atomic PS 15 spectrometer operating at 25 MHz. Measurements were performed over a temperature range of 84–290 K, with the paramagnetic Q_2CuBr_4 phase measured from ~145 K to 290 K. Spin–lattice relaxation times (T_1) were determined using a saturation recovery method with a sequence of π/2 pulses, followed by a variable delay time (τ) and a reading π/2 pulse. The second moment (M_2) of the ^{1}H NMR line was measured in the 109–290 K range using a continuous-wave ELLAB TEL-Atomic CWS 12-50 spectrometer operating at 28.2 MHz. M_2 values were calculated *via* numerical integration of the derivative of the absorption signal. Non-exponential magnetization recovery was observed across the entire temperature range. Low temperatures were achieved using liquid nitrogen vapor, with temperature regulation provided by a UNIPAN 660 controller equipped with a Pt100 sensor, ensuring long-term temperature stability within ±1 K. Powdered samples were sealed under vacuum in glass ampoules after evacuation at room temperature. All measurements were performed during heating. The estimated error in T_1 measurements was approximately 5%.

Theoretical calculation

Five functionals were employed to calculate the Q_2CuBr_4 subunits in fixed experimental and in optimized geometries: B97D, the Grimme's functional including dispersion,[23] Minnesota type, the M06 – global hybrid functional with 27% HF exchange,[24] and the M06-L, the local functional, with 0% HF exchange[25] the LC-TPSSTPSS, *meta*-GGA with long-range correction.[26,27] The calculations included scalar relativistic correction by DKH. The Jorge-DZP-DKH[28] basis set has been used. The calculations of the unit cells composed of four Q_2CuBr_4 sub-units, were conducted using long-range corrected metaGGA functional LC-TPSSTPSS, at non-relativistic, scalar relativistic and spin–orbit relativistic levels. The double-ζ and triple-ζ basis sets, such as Jorge-DZP,[28] Jorge-DZP-DKH,[28] Jorge-TZP[29,30] and Jorge-TZP-DKH[31] has been employed respectively. All unit cells were superimposed, thus have corresponding orientation and atomic positions. The computations have been performed with Gaussian 16.[32]

IR spectroscopy

The temperature-dependent infrared spectra were measured in a heating mode on a KBr pellet in the range of 4000–550 cm^{-1} using a Nicolet iN10 Fourier transform IR spectroscopy microscope equipped with a ZnSe-Linkam cryostat cell THMS600 with a temperature stability of 0.1 K, liquid nitrogen (LN2) cooled mercury–cadmium–telluride detector, permanently aligned 15× objective, 0.7 numerical aperture with the working distance set at 16 mm. The spectral resolution was set at 2 cm^{-1}.

We made attempts to collect Raman spectra, however, it turned out impossible due to high-intensity luminescence when exciting the sample with 488, 514, 830 or 1064 nm.

3. Results and discussion

Phase transition

The differential scanning calorimetry (DSC) technique was used to investigate the phase transition behavior of Q_2CuBr_4. As shown in Fig. 1a, the DSC results reveal a reversible structural phase transition, characterized by an endothermic peak at 297 K and an exothermic peak at 293 K, with a small thermal hysteresis of approximately 5 K between the heating and cooling processes. For clarity, the phases below and above the transition temperature are labeled as the low-temperature phase (LTP, Phase II) and high-temperature phase (HTP, Phase I), respectively.

The calculated entropy change (ΔS) of Q_2CuBr_4 is approximately 8.89 J mol^{-1} K^{-1}. According to the Boltzmann equation, $\Delta S = R \ln N$ (where N represents the number of distinguishable geometric orientations allowed in phases I and II), the estimated value of N is about 2.86, suggesting that Q_2CuBr_4 undergoes an order–disorder phase transition. Additionally, multiple cycles of cooling and heating DSC measurements at a scanning rate of 10 K min^{-1} were performed to confirm the thermal stability of the Q_2CuBr_4 compound (Fig. 1b). The results indicate that after several endothermic and exothermic cycles, both the phase transition and the magnitude of the heat flow remain consistent. This suggests that the material could potentially be utilized as a thermal switch in future applications.

Structure analysis

The Q_2CuBr_4 crystalizes in the $P2_1/c$ symmetry at RT and is isostructural with previously described structures of Q_2MBr_4 (where M = Co, Mn, Cd)[16] and Q_2CuCl_4 [11] at RT. The asymmetric unit consists of two organic cations, Q, and one tetrabromocuprate(II) anion, $CuBr_4{}^{2-}$ (Fig. S1b). One Q ion (Q1) is ordered in phase I, while the other (Q2) is disordered over two positions, similar to observations at RT in Q_2MBr_4 and Q_2CuCl_4. However, the behaviour of Q2 in Q_2CuBr_4 differs from that in the other compounds. Here, the disorder results from rotation around the axis formed by N2 and C14 atoms (see Fig. S2), rather than tilting, as in the earlier structures. As

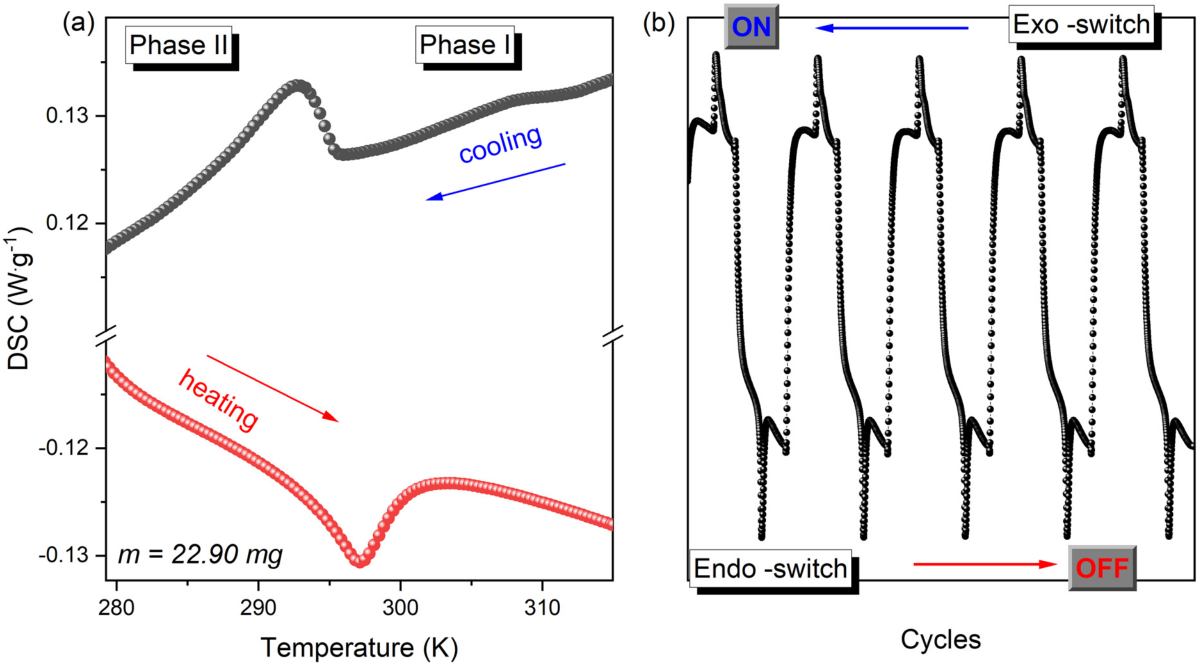

Fig. 1 (a) DSC curves of Q_2CuBr_4 in heating/cooling run; (b) DSC cycle test of Q_2CuBr_4 with a scan rate of 10 K min^{-1}.

a result, there are fewer distinct N–H⋯Br bonds in the structure. The Q2 ion and $CuBr_4^{2-}$ are connected by N2–H2⋯Br1 bond, with H⋯Br distance of 2.43 Å (Table S1), notably shorter than in other compounds: 2.81–2.87 Å (Q_2CoBr_4), 2.46–2.56 Å (Q_2MnBr_4), 2.46–2.76 Å (Q_2CdBr_4), and 2.52–2.64 Å (Q_2CuCl_4).

After PT to the low temperature phase II, the Q_2CuBr_4 structure adopts the non-centrosymmetric *Pc* space group, with all atoms ordered. The position of Q2 in phase I splits into two distinct positions, Q2 and Q3 (Fig. 2 and Fig. S3), each occupying one of the previously disordered positions. This leads to the loss of the two-fold screw axis and a reduction in symmetry. In phase II, polarization can occur along all directions except the unique axis. The asymmetric unit contains four Q cations (Q1–Q4) and two inorganic anions (Fig. S2). There are now two HBs corresponding to N2–H2⋯Br1 bond in phase I: 2.41 Å for N2–H2⋯Br1 and 2.46 Å for N3–H3⋯Br5.

To identify features distinguishing Q_2CuBr_4 from analogous structures, we focused on polyhedral distortions. The intermolecular interactions cause angular and bond length distortions of the tetrahedra, most pronounced in Q_2CuBr_4 (Table 2). This is confirmed through polyhedral angle variance (σ^2) and bond length distortion (Δ) values (calculated with VESTA[33]), as well as the distance between the M^{II} ion and the tetrahedral centre of gravity (d_G), the Σ parameter (sum of deviations from the ideal angle of the six *cis* angles in the coordination sphere of the metal ion), and the structural parameter (τ'_4), which describes the coordination geometry.[34] All data are in Table 2.

Table 2 shows that σ^2 and Σ values are significantly higher for Q_2CuBr_4 than in other bromine-containing compounds, indicating more pronounced angular distortions. Although Q_2CuCl_4 shows comparable angular distortions in its low-temperature monoclinic phase II, its orthorhombic phase I exhibits less distortion than the monoclinic phase I of Q_2CuBr_4. This suggests greater strain in the copper coordination environment of Q_2CuBr_4.

Additionally, the Δ values for Q_2CuBr_4 are among the highest, indicating significant bond length distortions. Comparing Cu–Br bond lengths in the two phases reveals stronger distortion in phase I (2.363/2.370–2.412 Å) than in phase II (2.360–2.400 Å; Table S2). This is consistent with the more pronounced geometrical distortion in Q_2CuBr_4 due to the Jahn–Teller effect, which is particularly significant for Cu^{2+} compared to other transition metals. In contrast, the other Q_2MX_4 structures typically exhibit much lower Δ values, reflecting less distorted coordination environments.

Meanwhile, the d_G values for Q_2CuBr_4 are among the smallest, suggesting that despite angular distortions, the copper-based structures exhibit the smallest deviation from the tetrahedral centre of gravity, even though the geometry remains far from ideal. This means that Q_2CuBr_4 maintains a more compact and rigid coordination environment despite the significant distortions in bond lengths and angles. Interestingly, Q_2CuCl_4 has the lowest d_G value, implying an even closer approach to ideal tetrahedral geometry and less geometric strain. Both copper-containing compounds (Q_2CuBr_4 and

Table 2 Comparison of tetrahedral distortion parameters: d_G, bond length distortions (Δ), tetrahedra angle variance (σ^2), Σ and τ'_4 parameters for Q_2MX_4 (M^{II} = Co^{2+}, Mn^{2+}, Cd^{2+}, Cu^{2++}; X = Br, Cl)

Structure	Phase, space group	T (K)	d_G	Δ ($\times 10^{-2}$)	σ^2 (deg^2)	Σ	τ'_4
Q_2CoBr_4[16]	**II**, $P2_1/n$	100	0.045	0.24	10.9	16.6	0.95
	I, $P2_1/c$	295	0.046	0.28	14.3	19.7	0.94
Q_2MnBr_4[16]	**II**, $P\bar{1}$	100	0.077	0.82	27.0	25.5	0.91
			0.033	0.20	35.9	29.0	0.90
	I, $P2_1/c$	295	0.058	0.34	19.1	23.1	0.93
Q_2CdBr_4[16]	**II**, $P2_1/c$	295	0.070	0.46	25.2	26.6	0.92
	I, *Pmcn*	365	0.057	0.27	11.4	14.7	0.94
Q_2CuBr_4	**II**, *Pc*	100	0.039	0.58	288.7	85.6	0.67
			0.048	0.72	271.4	83.0	0.68
	I, $P2_1/c$	300	0.041	0.53	261.7	81.4	0.68
Q_2CuCl_4[11]	**II**, $P2_1/c$	100	0.018	0.41	280.3	84.1	0.68
		295	0.018	0.41	286.7	85.0	0.68
	I, *Pnma*	365	0.030	0.75	183.5	68.1	0.74
Q_2CoCl_4[11]	**II**, $P2_1/n$	100	0.051	0.26	16.3	20.4	0.97
		295	0.054	0.43	10.6	16.4	0.95
	I, *Pnma*	340	0.052	0.56	3.1	8.2	0.94
Q_2MnCl_4	**II**, $P2_1/c$	260	0.040	0.28	23.5	24.1	0.97
	I, *Pnma*	295	0.063	0.45	4.6	10.6	0.92

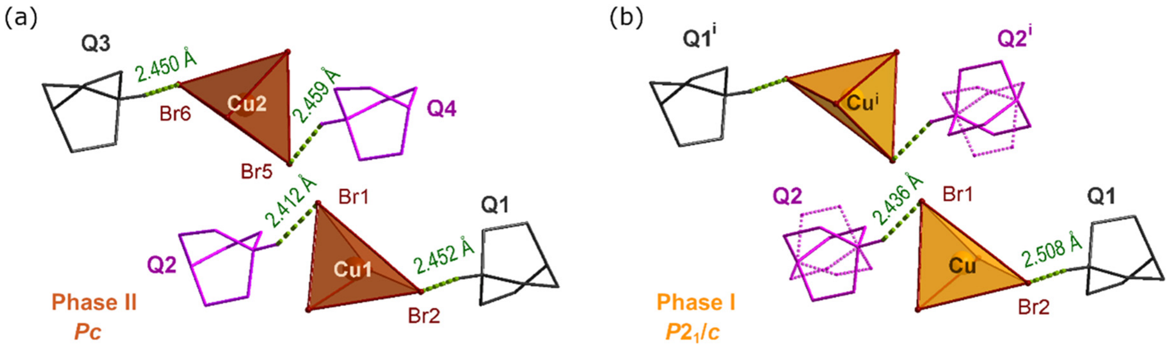

Fig. 2 (a) The Q_2CuBr_4 structure in phase II at 100 K showing $CuBr_4^{2-}$ anion with adjacent Q cations and N—H⋯Br bonds presented as green dashed lines. (b) The Q_2CuBr_4 structure in phase I at 300 K. The disordered Q2 cations are presented with pink dotted lines. The symmetry code: (i) $-x + 1, -y + 1, -z + 1$.

Q_2CuCl_4) deviate most from ideal tetrahedral geometry, but Q_2CuBr_4 shows more severe distortions, as indicated by its lowest τ_4' values. This suggests a more distorted coordination around Cu^{2+} in Q_2CuBr_4 than in Q_2CuCl_4. The larger Δ and σ^2 values in Q_2CuBr_4 reflect greater strain, likely due to the larger, more polarizable Br^- ions compared to Cl^- in Q_2CuCl_4. This highlights the role of halide size and polarizability in modulating structural properties and the degree of distortion in these copper-containing compounds.

Electrical and ferroelectric properties

A comprehensive analysis of complex permittivity (ε^*), electric modulus (M^*), and impedance ($Z^* = Z' - jZ''$) was carried out to investigate the electrical behavior of Q_2CuBr_4. Dielectric spectroscopy was employed to study dipolar switchability and molecular dynamics. The reorientation of quinuclidinium (Q) cations under an electric field induces a strong dielectric response. A characteristic λ-shaped anomaly near the phase transition temperature (T_c = 295 K) was observed across all frequencies, typical of a normal ferroelectric transition (Fig. 3a). The weak frequency dependence of ε' suggests that dipole moments follow the oscillating field, while the subtle shift of the peak at T_c confirms an order–disorder transition from the ferroelectric to paraelectric phase.

Periodic temperature cycling of the dielectric constant showed that both the switching period and signal intensity remained stable, confirming the thermal stability of Q_2CuBr_4 (Fig. 3b). Near T_c, the dielectric permittivity follows the Curie–Weiss law: $\varepsilon' = C_{\text{para}}/(T - T_0')$ or $\varepsilon' = C_{\text{ferro}}/(T_0 - T)$, as confirmed by the inset in Fig. 3a. The $C_{\text{para}}/C_{\text{ferro}}$ ratio of 1.4[35,36] and continuous cell volume changes (Fig. S4) indicate a second-order phase transition. Additionally, the fitted Curie temperature T_0 = 293.2 K (at 100 kHz) closely matches T_c, further supporting a second-order transition.

One of the most reliable measurements providing evidence of ferroelectric properties is the measurement of ferroelectric loop hysteresis. For this reason the polar properties of Q_2CuBr_4 were confirmed by the *P–E* hysteresis behavior. At higher temperature, just a few degrees below T_c, ferroelectric properties are disturbed by the conducting contribution. The polarization *vs.* electric field (*P–E*) hysteresis loop for lower temperature is displayed in Fig. 4 and clearly demonstrates the ferroelectric nature of Q_2CuBr_4.

The results indicate that the polarization increases with temperature, which may raise doubts and seems to contradict the basic *P–T* relation. Such dependencies may result from various conditions.[37,38] Firstly, none of the recorded *P–E* loops, although well defined, is fully saturated. At the same time, as polarization decreases with temperature, dipoles are easier to switch at high temperatures, which causes further increase in polarization. An application of larger fields would cause an increase in the polarization with complete saturation of the *P*–

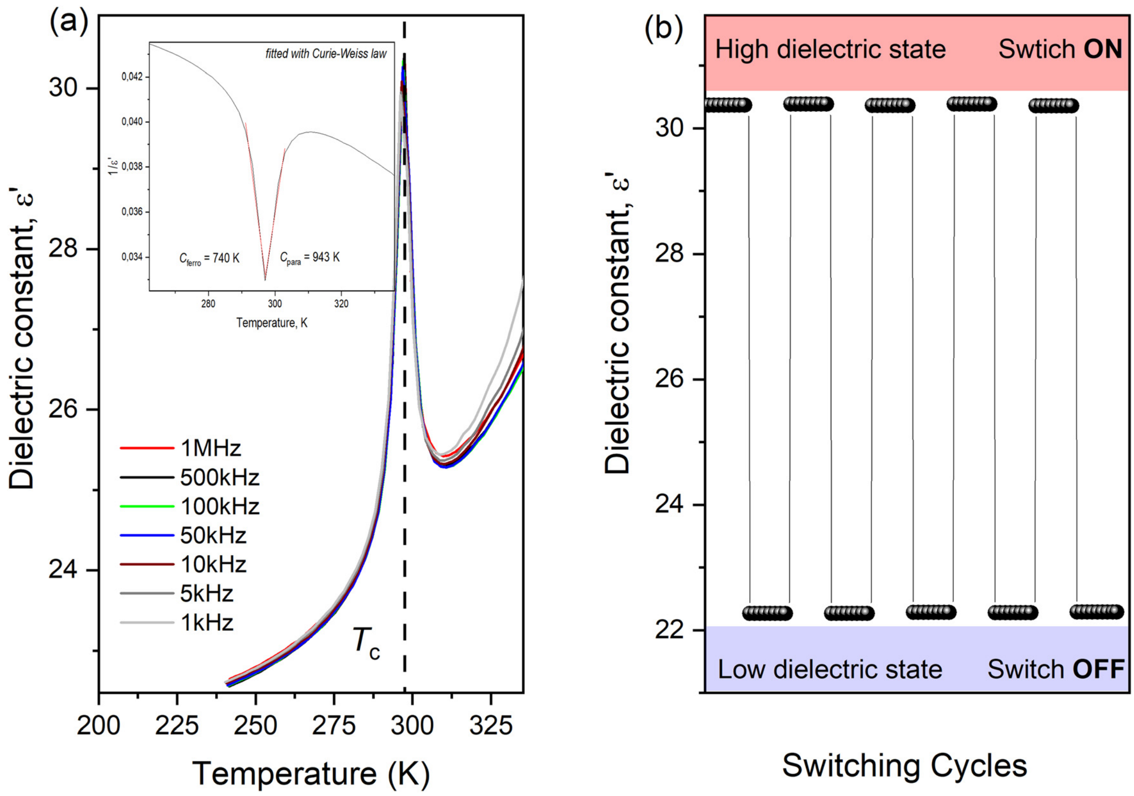

Fig. 3 (a) The temperature-dependent ε' of powder-pressed sample of Q_2CuBr_4 at selected frequencies. The insert shows the fitting to the Curie–Weiss law. (b) Reversible switching of the dielectric constant after multiple ON/OFF cycles at 1 MHz for Q_2CuBr_4.

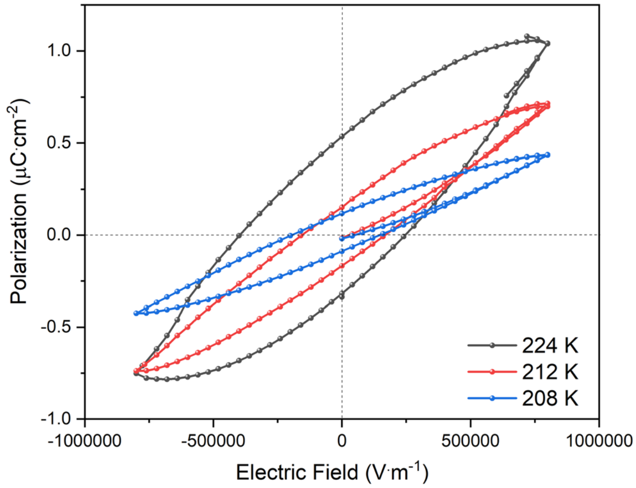

Fig. 4 The electric-field dependent ferroelectric hysteresis loops for a powder pressed Q_2CuBr_4 crystals measured at selected temperatures.

E loop and it is expected to see higher polarization with increasing temperature. Secondly, the conductivity of the Q_2CuBr_4 is significant at higher temperatures, which is manifested by the slightly curved tips of the hysteresis loops. The higher conductivity results in a decrease in polarization with increasing electric field strength, which is caused by the formation of leakage currents. Additionally, an internal bias can be created in the sample mainly due to some defects or domain wall pinning in the crystal. Due to the significant conductivity of the sample our attempts to use sample probing for piezoelectric and pyroelectric measurements were unsuccessful. In order to demonstrate nonlinear properties, alternative measurements of nonlinear electrical properties were used and discussed later in the paper.

The spontaneous polarization is defined as the ratio of the dipole moment per density of dipoles $P_s = \mu_s/N$, where $N = Z/V$ (see Table 1) and μ_s is the dipole moment taken from the theoretical calculation as a dipole moment of four dipoles of isolated sub-unit (Table S10, SI). For Q_2CuBr_4, P_s was estimated to be 0.659 μC cm^{-2}, which is consistent with the experimental value of P at $E = 0$. The origin of polarization in Q_2CuBr_4 is attributed mostly to the tetrabromocuprate anions, as they carry a permanent dipole moment due to Jahn–Teller distortion.[39] However, the Q cations themselves also possess a small dipole moment. In Q_2CuBr_4, both entities contribute to this phenomenon (Fig. S3). Q_2CuBr_4 crystals exhibit relatively small polarization values compared to other hybrid compounds, but despite the influence of conductivity, they are in agreement with theoretical predictions. A similar, relatively small value of polarization has been revealed and/or theoretically predicted in other organic–inorganic hybrids compounds, like *e.g.*, $[H_2dbco]_2Cl_3[CuCl_3(H_2O)]H_2O$,[40] dabcodo-LTa,[41] 1-propyl-1*H*-imidazole (PIm)[42] or even like a well-known Rochelle salts,[43] and much smaller than for *e.g.* $DMAGeI_3$.[44] It should be emphasized that the polarization value for Q_2CuBr_4 is also similar to other quinuclidine-based compounds, such as $HQReO_4$ [18] or (*R*)-(−)-3-hydroxyquinuclidinium chloride.[17]

Fig. 5a shows the frequency dependence of imaginary part of electric modulus (M'') for selected temperatures. It is clear that M'' *vs.* $\log(f)$ scans shows, in the entire analyzed frequency range, well define one maximum at each temperature. The fact that the peaks shift to higher frequency regions with increasing temperature suggests the accumulation of free charge at the interface, and indicates an increase in charge carrier mobility and a decrease in the relaxation time. Moreover, the shift of the peak $M_{\max}$ located at $f_{\max}$ towards higher frequencies as the temperature increases indicates that dielectric relaxation is thermally activated. The plot of $\ln(f_{\max})$ as a function of $1000/T$ conforms to Arrhenius' law as depicted in Fig. 5b. The calculated activation energies are $E_{a1} = 1.07$ eV (for $T > T_c$) and $E_{a2} = 0.69$ eV (for $T < T_c$). These values are closely aligned to those obtained from DC conductivity analyses also presented in Fig. 5b, suggesting that the transport of the charge carriers in the studied structure is done by the same process, which is a hopping mechanism.[45,46] In the studied compound, Q_2CuBr_4, the DC conductivity value equals 2.8×10^{-11} S cm^{-1} at room temperature. The observed conductivity behavior indicates the presence of thermally activated transport across the investigated temperature range, with different proton hopping regimes likely dominating below and above the phase transition. The activation energy of 0.69 eV, obtained from DC conductivity and electric modulus (M'') analysis below the transition temperature (~290–300 K), could initially be interpreted as indicative of electronic hopping. However, structural and spectroscopic data confirm that copper exists solely in the +2 oxidation state, with no evidence for the presence of Cu^+ or mixed-valence states, effectively ruling out this mechanism. Therefore, the conduction process in this range is more plausibly attributed to localized motion, possibly limited by a less dynamic hydrogen-bonding environment. Upon heating and structural transformation, the activation energy increases to 1.1 eV, suggesting a transition to a long-range, thermally activated ionic transport mechanism. Although, relatively high for classical proton conductors, this behavior aligns with trends observed in other hybrid systems. For example, in the superprotonic compound $Rb_4(SO_4)(HSO_4)_2(H_3AsO_4)$, a similar increase in activation energy was observed with temperature, rising from ~0.58 eV to 0.9 eV after the phase transition. The authors attributed this to the formation of a more ordered hydrogen-bond network, which, while enabling faster proton transfer, also imposed higher energy barriers due to stronger, more structured interactions.[47] After the phase transition, the ordering of the quinuclidinium sublattice and the presence of well-defined N–H⋯Br hydrogen bonds (as short as 2.41 Å) could support efficient but energetically demanding proton hopping. Similar mechanisms have been reported in other hybrid halide systems, such as $[4\text{-AQ}]_4Cu_4Cl_8$,[48] $(C_3H_8N_6)_2ZnCl_4\cdot 2Cl$,[49] and $[C_{13}H_{16}N_2]_5(BiCl_6)_3Cl$,[50] all of which rely on hydrogen-bond-mediated proton conduction.

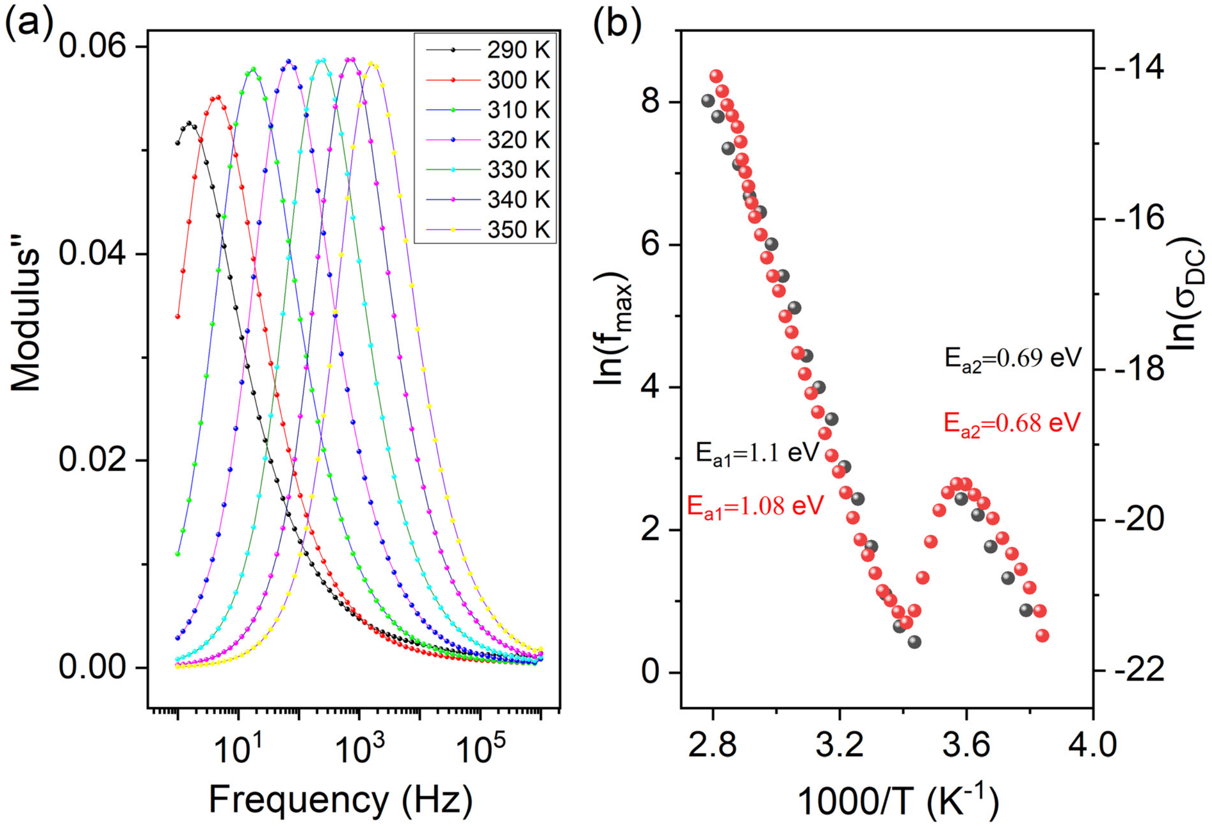

Fig. 5 (a) The variation of M'' as a function of the frequency log(f) at selected temperatures; (b) the evolution of f_{max} and σ_{DC} *versus* 1000/T and the determined activation energies for a given temperature in Q_2CuBr_4.

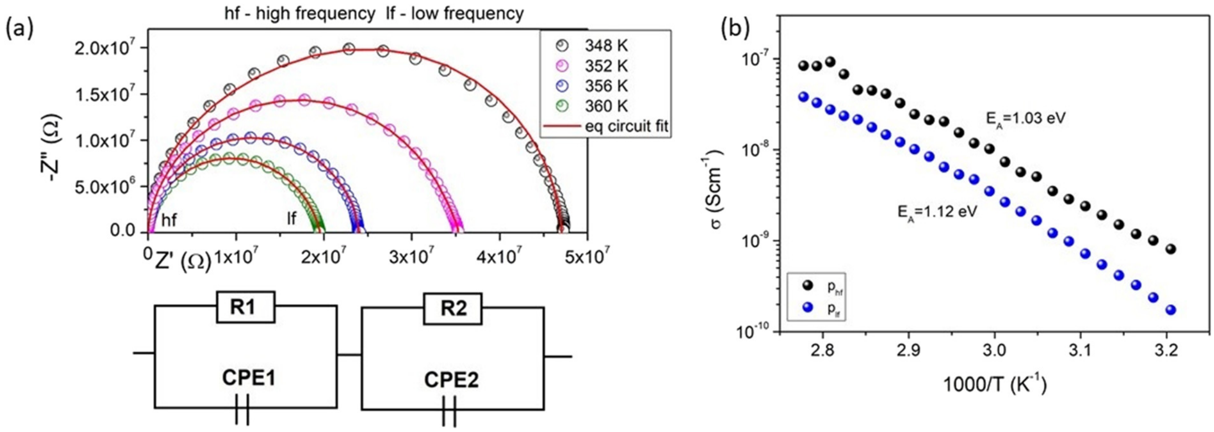

Fig. 6 (a) The Nyquist diagram spectra plotted against temperature together with electrical equivalent circuit fitting; (b) conductivity values estimated for two relaxation processes based on Nyquist plots fitting in Q_2CuBr_4.

The electrical properties were also studied by complex impedance spectroscopy, a powerful method that allows the separation of electronic and ionic conduction. Fig. 6a shows the Nyquist diagrams (Z'' *versus* Z') of the Q_2CuBr_4 compound at selected temperatures. Since the plot presents a single but asymmetric and flattened semicircle at all temperatures, it was concluded that two highly overlapping relaxation processes are present. Each process was modeled by a resistor connected in parallel with a constant phase element (CPE) and the resulting components were then connected in series. The impedance of a single process is described by the formula:[51,52] $Z = R/[1 + RQ_{CPE}(j\omega)^n]$, where R represents the resistance, Q_{CPE} is the CPE parameter, n is the exponent characterizing the non-ideal capacitive behavior ($0 \le n \le 1$),

ω is the angular frequency, and j is the imaginary unit. In the case where $n = 1$, the CPE behaves like an ideal capacitor with capacitance $C = Q_{\mathrm{CPE}}$. This model yielded the best fitting results, as indicated by the solid lines in Fig. 6. Fig. 6b compares the conductivity values estimated from the resistivity of both processes (R_1, R_2). These processes are labeled as "hf" for the high-frequency process and "lf" for the low-frequency process. Although both processes occur in the high-temperature phase (above the structural phase transition T_c), they exhibit distinct characteristics. The hf process is characterized by higher conductivity and a stable value of the CPE exponent $n \approx 0.98$ across the entire studied temperature range (312–360 K), indicating nearly ideal capacitive behavior. In contrast, the lf process shows lower conductivity, a higher activation energy, and a gradual decrease in the n parameter from 0.98 to approximately 0.92 with increasing temperature, suggesting a growing dispersion in the relaxation behavior. Both observed processes are attributed to protonic conduction, occurring in different structural or microstructural environments within the same phase. The hf process likely corresponds to fast, localized proton hopping within the bulk structure (*e.g.*, *via* dynamic N–H⋯Br or/and C–H⋯Br hydrogen bonds), while the lf process may reflect more hindered proton transport, affected by interfacial regions, defects, or accumulation at the electrode interfaces. This interpretation is further supported by the Q_{CPE} values extracted from the model. For the hf process, Q_{CPE} remains low and only slightly increases with temperature (6–8×10^{-12} F), consistent with low capacitance and the absence of charge buildup. In contrast, Q_{CPE} for the lf process increases significantly with temperature, reaching values near 2×10^{-11} F at 360 K, indicative of ion accumulation at interfaces and growing capacitive effects. Finally, the activation energies of both processes are comparable to the activation energy extracted from DC conductivity measurements, confirming that proton transport is the dominant mechanism in both relaxation processes, albeit operating in structurally distinct regimes.

Nonlinear electrical effects

The study of nonlinear electrical properties provides insights into charge transport mechanisms, ion dynamics, and deviations from linear conduction behavior, with higher-order conductivity components revealing processes linked to intrinsic nonlinearities and nonstationary effects.[53,54] Analyzing their frequency dependence further uncovers features of ion hopping, electrode polarization, and conduction anisotropy, often hidden in standard low-voltage (1 V) linear studies.[55,56] To determine whether a material exhibits nonlinear behavior, it is essential to assess the contribution of higher harmonics in the conductivity response, usually explored at substantially higher voltages. A useful approach is to analyze the ratio of the third harmonic conductivity to the base conductivity, presented in Fig. 7a. The ratio for the investigated compound varies between 0.26 and 0.295, indicating a nonlinear contribution above 25% that suggests strong deviations from linear charge transport, likely associated with ion dynamics and charge transfer processes.[57] This clearly shows that, in the case of Q_2CuBr_4, nonlinear components that can be attributed to its intrinsic properties appear already at very low voltages, close to 3 V. In most organic–inorganic hybrids, ferroelectricity originates from the orientational order–disorder dynamics of the organic cations. In Q_2CuBr_4, this involves the quinuclidinium cation, whose orientation relative to the $[CuBr_4]^{2-}$ anionic lattice determines the polarization. In such systems, the barriers to cation reorientation are low, since these involve only molecular rotations, rather than large displacements of heavy ions such as Ti^{4+} and O^{2-} in classical perovskites like $BaTiO_3$ or $PbTiO_3$. Consequently, in hybrid ferroelectric Q_2CuBr_4, the quinuclidinium reorientations are local and energetically much easier; therefore, it exhibits nonlinear response under comparatively weak fields.

During heating, the third harmonic conductivity content increases with temperature, reaches a maximum, then decreases before exhibiting another peak around 300 K. During cooling, the third harmonic content generally decreases with increasing temperature, although a small maximum is observed around 290–300 K. The positions of these anomalies align with the DSC results, indicating the presence of a phase transition and a significant increase in electrical permittivity. The results are presented for an example frequency of 1 Hz, but they closely overlap with those obtained at higher frequencies, as shown in Fig. 7b. It can be observed that, for a given temperature during heating or cooling, fluctuations in the ratio reach a maximum of 0.004 within the frequency range of 1 Hz to 100 Hz. The magnitude of the difference remains the same regardless of whether the temperature is below or near the phase transition. This variation is negligible compared to the overall values in the range of 0.25–0.29. For this reason, the results obtained at a frequency of 1 Hz will generally be presented in further analyses.

The values of the real part of the base and third harmonic current density, $j'_{3\mathrm{h}}$ and $j'_{1\mathrm{h}}$, were determined based on relations $j'_{3\mathrm{h}} = \sigma'_{3\mathrm{h}}E_0$ and $j'_{1\mathrm{h}} = \sigma'_{1\mathrm{h}}E_0$.[57] Fig. 7c shows the obtained values as a function of temperature during cooling at frequencies of 1 Hz and 100 Hz. The study of these parameters confirms the occurrence of a phase transition around 290–300 K in the tested compound. This is evidenced by a maximum in the third harmonic current density, observed at both 1 Hz and 100 Hz. A similar maximum is also present in the first harmonic current density, as shown in the inset of the figure. During heating, an inflection point is also visible near the phase transition, although it appears more flattened. The analysis of the conductivity ratio $\sigma'_{3\mathrm{h}}/\sigma'_{1\mathrm{h}}$ and the temperature-dependent behavior of the current density harmonics support the hypothesis of a phase transition around 290–300 K. This phase transition likely enhances ion mobility, particularly for bromide ions, contributing to the observed maxima in the third harmonic current density. Additionally, electrode

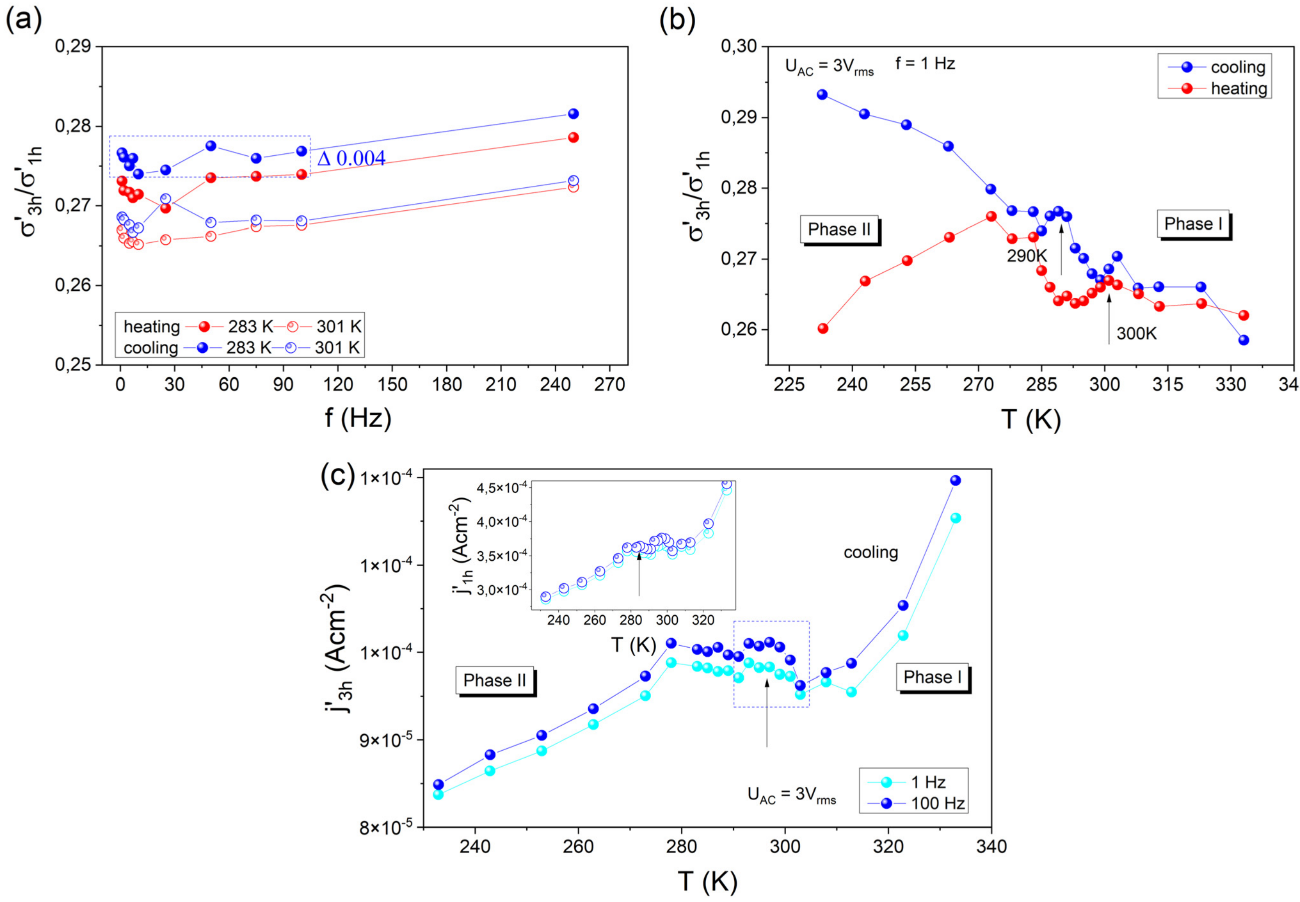

Fig. 7 The ratio of the real part of the third harmonic conductivity ($\sigma'_{3h}/\sigma'_{1h}$) to the base one as a function of (a) temperature at a frequency of 1 Hz, and (b) frequency at temperatures of 283 K and 301 K, measured during heating and cooling. (c) The real part of the third harmonic current density as a function of temperature measured during cooling at frequencies of 1 Hz and 100 Hz. The inset presents the first harmonic current density under the same conditions.

effects, such as ion accumulation at interfaces, become prominent at low frequencies and high temperatures, influencing the nonlinear response.

In the literature, nonlinear properties are also described using alternative approaches, such as higher-order conductivity coefficients, which provide additional insights into the material's complex electrical behavior[58]

$$j' = \sigma'_{10}E_0\cos(\omega t) + \sigma'_{20}{E_0}^2\cos^2(\omega t) + \sigma'_{30}{E_0}^3\cos^3(\omega t) + \ldots \quad (3)$$

Here the σ'_{10} is linear conductivity, and σ'_{20}, σ'_{30} *etc.* are higher-order conductivity coefficients. By comparing both eqn (1) and (3) and utilizing Fourier transforms, it is possible to calculate the higher-order conductivity coefficients.[59,60] The analysis of the third-order conductivity coefficient (σ'_{30}) provides valuable insights into the conduction mechanism within the material. This parameter helps distinguish between different types of charge transport, including ionic and electronic conduction, as well as correlated ion hopping dynamics.[59] The temperature dependence of σ'_{30} is presented in Fig. S5, SI, showing positive values across the entire measured temperature range for both heating and cooling. The consistently positive sign of σ'_{30} indicates that the conduction mechanism is likely not related to correlated back-and-forth ionic hopping, which would typically result in a sign change.[59,60] Instead, this behavior suggests a more unidirectional or electronic conduction process, possibly involving charge transfer between metal ions or a mechanism with free ion movement without strong correlation. The temperature dependence of the real part of the third-order electric susceptibility coefficient (χ'_{30}) provides valuable information for distinguishing the type of phase transition (see Fig. S5c, SI). For a continuous phase transition, χ'_{30} typically changes sign during heating, whereas for a discontinuous transition, there is no sign change.[57–59] Throughout the entire measured temperature range, no sign change of the χ'_{30} was observed. This consistent positive sign indicates that the phase transition in the Q_2CuBr_4 is of a discontinuous nature. A discontinuous, or first-order phase transition, is typically characterized by a distinct peak in the DSC thermogram, indicating the absorption or release of heat during the phase change which is in line with our results. A comparison between Q_2CuBr_4 and our previously reported imidazolate-azide-based Mn and Cd compounds[61] highlights both similarities and key differences in their nonlinear electrical behavior. In both studies, pronounced nonlinear dielectric effects were observed in the vicinity of a temperature-induced phase transition. In the earlier work, the phase transition was associated with changes in local symmetry and conductivity, and accompanied by enhanced nonlinear polarization effects, particularly in Mn^{2+}, where the third harmonic contribution reached up to 8%. However, despite these nonlinearities and thermally activated conductivity, no evidence for ferroelectric behavior (such as spontaneous polarization or hysteresis) was found. In contrast, Q_2CuBr_4 exhibits a well-defined structural phase transition near 290–300 K, which is strongly coupled to both calorimetric and dielectric anomalies as well as nonlinear electric response. The third harmonic reaches values as high as ~29%, and the behavior of the dielectric permittivity, electric modulus, and frequency-dependent conductivity all suggest cooperative dipolar dynamics, consistent with a ferroelectric-like transition. Furthermore, the mechanism of charge transport in Q_2CuBr_4, governed by proton hopping across strong N–H⋯Br hydrogen bonds, differs from the mixed conduction and more diffuse dipolar behavior observed in the Mn/Cd systems.[61] Thus, while both materials show nonlinear dielectric phenomena coupled to structural phase transitions, only Q_2CuBr_4 demonstrates a clear indicator of ferroelectric-like order, with its nonlinearity values being significantly higher.[61]

NMR study

T_1. The temperature dependence of the ^{1}H NMR spin–lattice relaxation time, T_1, for studied bromide compounds Q_2CuBr_4 is shown in Fig. 7a. The measured one-exponential magnetisation recovery functions for each point were only detected. For Q_2CuBr_4, the measured T_1 values were very short and close to the limit of measurement possibilities of such short times of the used spectrometer, probably due to the domination of strong paramagnetic interaction in the samples. Below 140 K no signal of FID was detected. Despite this limit uncertainty of experiment, we have used an approach to analysis already used previously for studied by us for the paramagnetic sample.[16] In the case of a predominant paramagnetic interaction the proton-proton dipol–dipol interaction may not be important and neglected. For final fitting procedure, we apply the simplified expression for the ^{1}H spin-lattice relaxation time[16,26] and the obtained dynamic parameters from the fitting procedure were as follows: E_{a1} = 6.46 kJ mol^{-1}, K_1 = 4.88 × 10^{11} Hz^2, as shown in Fig. 8a as theoretical line.

$$\frac{1}{T_1} = K_1 \frac{\tau_c}{1 + \omega_H{}^2 \tau_c{}^2} \tag{4}$$

M_2. The temperature dependence of the second moment, M_2, of the ^{1}H NMR line for paramagnetic Q_2CuBr_4 is presented in Fig. 8b. For studied Q_2CuBr_4, two close reductions are visible. The first, from ~22 × 10^{-8} T^2 in lowest temperatures, *via* the distinct threshold ~14 × 10^{-8} T^2 at about 130 K, and

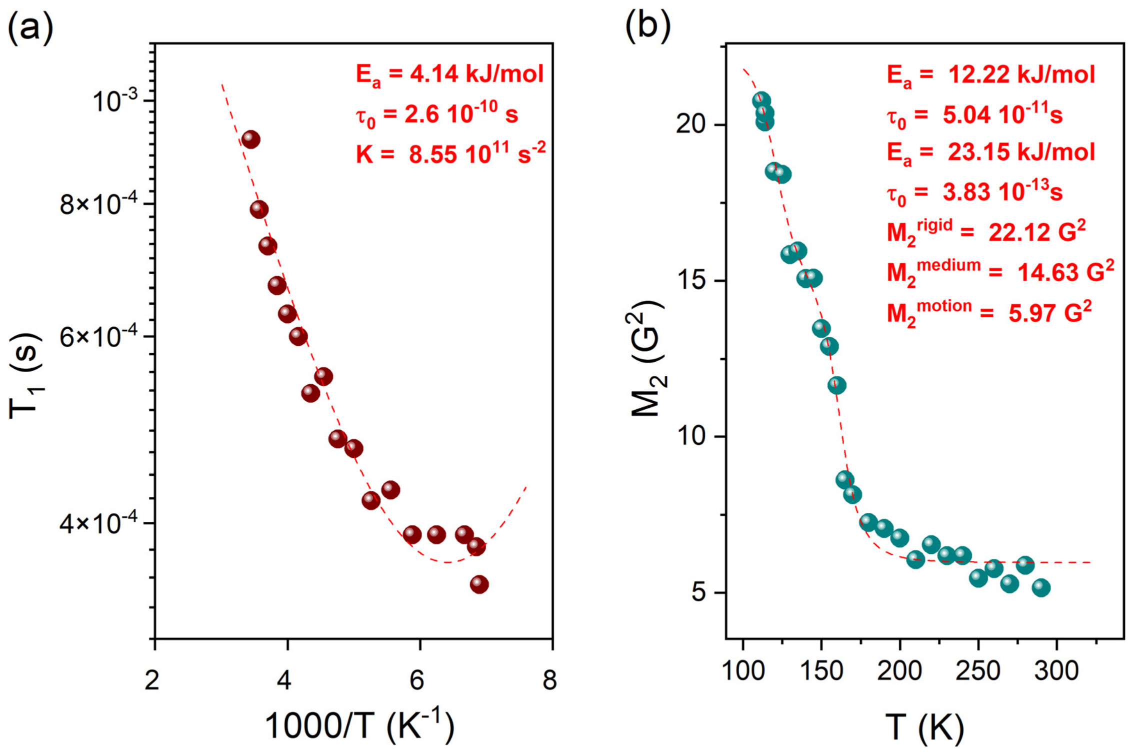

Fig. 8 (a) Temperature dependence of the proton spin–lattice relaxation time measured at 25 MHz. (b) Temperature dependence of the second moment of the ^{1}H NMR lines for Q_2CuBr_4.

then next down, decrease up to approximately 6 × 10^{-8} T^2 in region above 170 K. The theoretical calculation of the second moment for the rigid state of quinuclidinium molecular structure, based on structural crystallographic data, was previously performed in papers describing the chloride and bromide analogue compounds[11,16] with assumed distance between proton and carbon or nitrogen positions (C–H – 1.09 Å) and (N–H – 1.04 Å), giving $M_2^{\text{rigid}} = 18.06 \times 10^{-8}\,\text{T}^2$ (only *intra* value without considering *inter* value). Higher values at the lowest temperatures may be caused by the possible dipole–dipole interaction of protons with unpaired electrons in the QCuBr$_2$, the influence of the additional interaction of protons with the unpaired electron can be observed and, therefore, the measured total M_2 at the lowest temperatures is larger than that calculated for the rigid molecule. For calculation of dynamic parameters of the sequence of two found reductions of the second moment of ^{1}H NMR line, the following BPP formula was applied:

$$M_2 = \Delta M_2(1)\frac{2}{\pi}\tan^{-1}(\gamma_{\text{H}}\tau_{\text{c}}\sqrt{M_2}) + \Delta M_2(2)\frac{2}{\pi}\tan^{-1}(\gamma_{\text{H}}\tau_{\text{c}}\sqrt{M_2}) + M_2^{\text{motion}}, \tag{5}$$

where $\tau_{\text{c}} = \tau_0 \exp(E_{\text{a}}/RT)$, M_2^{rigid} (where $M_2^{\text{rigid}} = \Delta M_2(1) + \Delta M_2(2) + M_2^{\text{motion}}$) and M_2^{motion} are the second-moment values of both second moment reductions, respectively.

From the fitting, the following parameters have been obtained: in present case of Q$_2$CuBr$_4$, where it has been possible to determine the dynamic parameters of two reductions: first – E_{a1} = 12.22 kJ mol^{-1} and τ_{c10} = 5.04 × 10^{-11} s; and second – E_{a2} = 23.15 kJ mol^{-1} and τ_{c20} = 3.83 × 10^{-12} s (see theoretical dashed line in Fig. 8b). These both reductions, by practically the same amount, suggest a dynamic inequivalence of the quinuclidine cations in crystallographic structure in the ratio 1 : 1, and are consistent with the structural results. Above 170 K, after of both fitted reductions of M_2, the value stabilises to be about 6 × 10^{-8} T^2 s, significantly above the expected value for the cation tumbling. It should therefore be assumed that the cation performs some axial movement of quinuclidine cations and will probably start rotating at higher temperatures.

IR spectroscopy

We present a set of IR spectra as the function of temperature for Q$_2$CuBr$_4$ (Fig. S6). Table S12 contains the observed IR wavenumbers along with the assignment. The symbols used in the text have been explained in the footnote of this table. The assignment is based on the data available for the compounds containing Q and similar cations (*e.g.* dabco) and metal halides, specifically referring to the family of QMCl (quinuclidinium-metal chlorides) and QMBr (analogous bromides).[10,11,16] The observed modes originate from internal vibrations of the organic cations. The temperature-induces changes for selected modes are presented in Fig. 9. As determined by X-ray diffraction, the crystal undergoes a PT from $P2_1/c$ to Pc below 290 K on cooling. The transition probed by the measurements described above indicates a rather mixed order–disorder mechanism. The observation of IR spectra gives some further hints about the PT. The HBs, which are of medium strength with a center of gravity of stretching N–H modes located at 3060 cm^{-1} at RT, shift rather insignificantly with temperature increase by *ca.* 20 cm^{-1} towards higher wavenumbers (Fig. 9a and b). This is in contradiction to the other Q-metal-bromides where the shift was within 30–120 cm^{-1}, the highest value being exposed in Q$_2$CoBr$_4$.[16] It is also surprisingly small when compared to Q$_2$CuCl$_4$ sample, in which the shift was almost 150 cm^{-1}.[11] In the two latter examples the shift was explained by a high degree of order at LT and extremely high degree of disorder above PT resulting from almost unperturbed rotation of Q cations. In this case the small shift is the indication of not so violent Q-cations movement with a more uniform arrangement of HBs in HT. It can be clearly seen in Fig. 9b that the ordering, however, takes place throughout all the temperature range and the PT is noticeable only as a point at which the slope of the curve changes. The same refers to the full width at half maximum (fwhm). Its change is continuous and PT is marked as a small indentation in the curve with a slope increase. Further, the fwhm value of νNH band is small at LT, reaching roughly 40 cm^{-1}, being lower than in Q$_2$CuCl$_4$ – 120 cm^{-1} (ref. 11) and much lower than in other Q-metal-bromides with fwhm equal to 260 cm^{-1},[16] which again testifies their quite uniform organization in Q$_2$CuBr$_4$. The fact that both parameters: wavenumber and fwhm, alter without a tendency to certain limits with T increase, as well as the fact that the PT is manifested in IR spectra below the T_{c}, demonstrates that the mechanism is not governed by the reorganization of HBs, but rather HBs readjust to conform to the new quinuclidinium positions.

The PT is dependent mostly on the movement of quinuclidium cations as a whole, which confirms the findings from other characterization techniques. This is clearly seen in the case of absorption bands of Q internal vibrations. Both the stretching, bending and deformation modes are split below PT into two: for example the ν_{as}CH$_2$ band at 2964 cm^{-1} (RT) is split into 2962 and 2971 cm^{-1} at LT (Fig. 9c); the ωCH$_2$ band at 1342 is split into 1344 and 1340 cm^{-1}, while the stretching skeleton band at 1039 cm^{-1} is present as two components at 1041 and 1037 cm^{-1}, and τCH$_2$ band at 1039 cm^{-1} is observed as a doublet at 968 and 963 cm^{-1} below PT. This doubling of bands below PT is the direct confirmation of X-ray diffraction data, according to which the asymmetric unit in phase II contains double the amount of ions compared to phase I. The splitting value, however, contained within a few cm^{-1} is much lower than in analogous Q$_2$CuCl$_4$ or other Q$_2$MBr$_4$[11,16] reaching up to 40 cm^{-1}. This means that the Q cations in Q$_2$CuBr$_4$ are similar to each other in terms of bond lengths and angles.

Although, indeed IR spectra prove the disordering of the Q cation into new positions below PT and its ordering above PT, the onset of the PT is detected ahead of T_{c} on heating, namely the changes in band positions start roughly around 250 K and end at *ca.* 300 K. This suggests that the adjustment of the Q cages takes some time and the final click-in of Qs into new positions results in new ferroelectric phase.

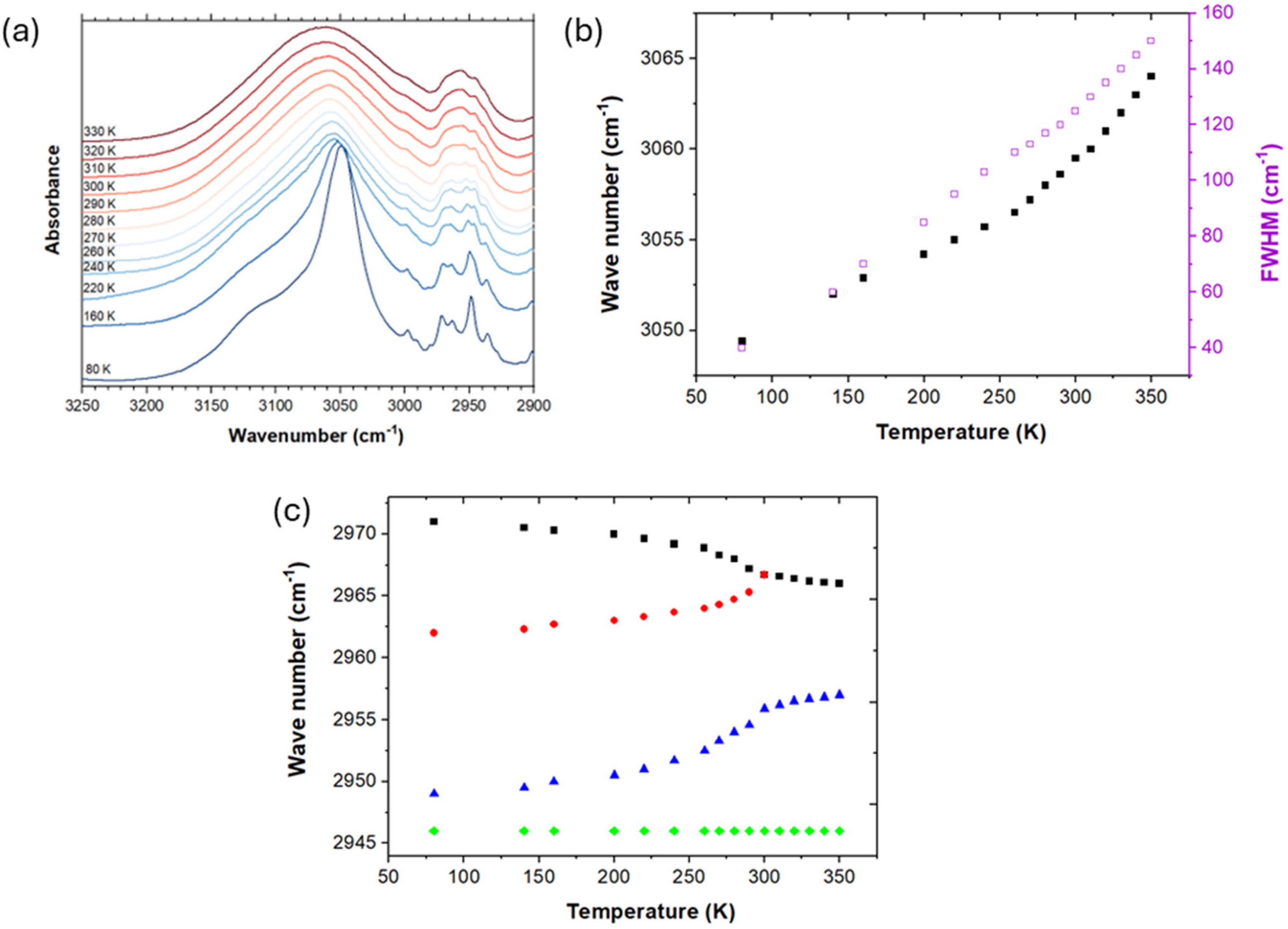

Fig. 9 (a) The details of IR spectra in the region of stretching N–H and C–H modes. The wavenumber (full figures) and their corresponding fwhm changes (empty figures) for (b) NH stretching, (c) CH_2 stretching modes.

Unfortunately, we have not been able to measure the Raman spectra, which would give us valuable information on the low-frequency vibrations, including the inorganic-network modes and quinuclidinium rotations/librations, and their contribution to the mechanism of PT, due to intense luminescence when exciting the sample with laser sources.

Theoretical results

Summary of results referring to energy gap, optical properties (dipole moment, polarizability, first order hiperpolarizability), NMR chemical shifts, UV-Vis spectrum, and DOS structure are presented here, with details provided in SI.

The LC-TPSSTPSS with double-ζ basis has been chosen as suitable computational method, based on the analysis of optimized and experimental geometries, relative energies, ionization potential, electron affinity and energy gap (see Table S3 and Validation of the Computational Method, and Basis Set Quality sections in SI). Theoretically estimated fundamental energy gapfor unit cell structures is expected not to be higher than ~6 eV (SI, section Energetics and Electronic Structure Characterization). The optical gap determined from Kohn–Sham eigenvalues is inconclusive. However, estimated using electric dipole polarizability, it is found at around 2.85 eV. This result is comparable with one obtained from experimental ferroelectric hysteresis, at zero field limit (Fig. 4), $(I-A)_{\mathrm{ex}} \propto \sqrt[3]{\frac{1}{\alpha_{\mathrm{ex}}}} \approx 2.87$ eV, and $\alpha_{\mathrm{ex}} \cong V\cdot\partial P_{\mathrm{S}}/\partial F$, where V is a normalized volume set to $(2a_0)$,[3] following simple order-of-magnitude estimate of physical constants used to describe the non-linear optical properties of materials,[62] with a_0 being Bohr radius, and F magnitude of electric field. The gap size suggests possible semiconducting nature. The atomic states contribution to frontier molecular orbitals has been determined with partial density of states, PDOS (Fig. S14 in SI). The HOMO levels are predominantly located on Br lone pairs, while the LUMO-β has mixed Cu/Br levels character. Notably, the higher in energy LUMO-α is localized on protons with small partial Cu character. Comparison with the aligned DOS of N and N ± 1 electron systems (energy shifted by $|\Delta| = 1.69$ eV, Fig. S15 in SI), shows that around chemical potential energy (corresponding to Fermi level) a state with Cu/Br mixed character resides. This mixed state is LUMO of cationic system (with dominant contribution from Br) or HOMO of anionic system (with predominant contribution from Cu). Because this state is found slightly below the chemical potential (mid between HOMO and LUMO), it is suggested that the material might have intrinsic or possible p-type semiconducting attributes. Further, a comparison between LTP and HTP phases *via* examination of polarizabilities allowed theoretically determining a 25° difference in charge transfer direction between LTP and HTP structures. The polarizabilities are further discussed in SI. The CT path is roughly along a line connecting Cu ions of neighbouring sub-units, thus more or less along vector sum of *a* and *b* lattice vectors. In isolated sub-units, the predicted charge transfer direction is almost parallel (~12°) with Q_2CuBr_4 dipole moment. All above indicates that CT direction is associated with H-bond interaction between Br^- and amine protons of quinuclidine. Moreover based on electric dipole moment and first-order hiperpolarizabilities the NLO behavior might be expected in LTP phase, since the LTP structure exhibits the intrinsic non-centrosymmetry, together with the non-zero dipole moment and large first-order hyperpolarizability values.

The assessment of relative theoretical NMR chemical shifts between high-spin (quintet) and low-spin (antiferromagnetic open shell singlet) states as well as between HTP and LTP structures illustrate electron shilding effects related to phase transition (Theoretical NMR Chemical Shifts section in SI). Between high-spin and low-spin configuration the change in chemical shifts is only meaningful for Br – upfield, and Cu – downfield shifts, estimated about 10 to 13 ppm absolute difference, Table S11 in SI. Therefore in high spin configuration Br ions are more shilded (electron rich), and Cu ions electron deshilded, which in terms of partial CT might be denoted as Cu $\xrightarrow{e}$ Br. The quinuclidine atoms show very small variability of chemical shifts in response to spin state configurations. Secondly, relative shifts between LTP and HTP are almost identical at each spin configuration. Chemical shifts are more sensitive to phase transition, thus the absolute change in shifts calculated as difference between the LTP and the HTP structures is much higher on average than variation resulting from the spin configuration. The greatest difference in calculated shifts, related to phase transition, is for Cu ions, Fig. S11 in SI. The three Cu ions are upfield shifted by over 150 ppm, and one is upfield shifted by ~ 60 ppm in HTP structures as compared to LTP structure. Therefore in HTP geometry the Cu ions become more shilded by electrons than in LTP structure. The remaining atoms in the system are generally downfield shifted. In terms of bond polarization it might be depicted through partial CT direction: Cu $\xleftarrow{e}$ Br in HTP *vs.* Cu $\xrightarrow{e}$ Br in LTP, and generally Q $\xrightarrow{e}$ $CuBr_4$. Also theoretical UV-Vis spectrum shows absorption change between HTP and LTP phase, resulting in maximum around the green and violet regions, Fig. S12 and S13 in SI. The difference between HTP or LTP unit cell curves and the sum of respective individual isolated sub-units curves indicates that the intermolecular interactions between the sub-units do not affect the absorption in visible region for HTP phase. However in LTP case the maxima around the green and violet regions appear, matching the change between HTP and LTP unit cell curves, which suggests that interactions between sub-units in LTP structure are responsible for increased absorption in the mid-range of visible electromagnetic spectrum (larger maximum corresponds to ~3.8 eV and lower one to ~5.1 eV).

4. Conclusions

In summary, (1-azabicyclo[2.2.2]octane)$_2$CuBr$_4$ with zero-dimensional perovskite hybrid architecture has been synthesized and examined for ferroelectric and switchable properties. The crystal structure of the compound was determined using XRD and its phase transition temperature is defined at 295 K. Its switchable electric polarization mainly originates from the dynamic ordering of Q cations and tetrabromocuprate anions moieties. Both NMR and IR spectroscopy provide variable information on the dynamics of the system around PT, specifically, the rearrangement of the hydrogen bonding. The switchable thermal and dielectric constant measurements have shown a high stability of this compound. Theoretical studies have enriched significant knowledge about the properties of the compound, confirming both quantitatively and qualitatively ferroelectric properties. This material, prepared by a simple method of evaporation of aqueous solution, can serve in its future applications as information storage, switchable or optoelectronic devices.

Conflicts of interest

There are no conflics to declare.

Data availability

All data analyzed in presented paper are included in this published article and its supplementary information (SI). Supplementary information: additional experimental details, XRD and Raman analysis, analysis and discussion of numerical simulations. See DOI: **https://doi.org/10.1039/d5dt01668a**.

Additional datasets used and/or analyzed during the current study are available from the corresponding author on reasonable request.

CCDC 2417202 and 2417203 contain the supplementary crystallographic data for this paper.[63a,b]

Acknowledgements

The work was supported by the project Minigrants for doctoral students of the Wroclaw University of Science and Technology. The author thank Wroclaw University of Science and Technology for financial support. This research was supported in part by the computational resources of the Wrocław Centre for Networking and Supercomputing, which are gratefully acknowledged.

References

1 A. Piecha-Bisiorek, A. Bieńko, R. Jakubas, R. Boča, M. Weselski, V. Kinzhybalo, A. Pietraszko, M. Wojciechowska, W. Medycki and D. Kruk, Physical and Structural Characterization of Imidazolium-Based Organic–Inorganic Hybrid: (C3N2H5)2[CoCl4], *J. Phys. Chem.*, 2016, **120**(12), 2014–2021, DOI: **10.1021/acs.jpca.5b11924**.

2 I. B. H. Sadok, F. Hajlaoui, K. Karoui, N. Audebrand, T. Roisnel and N. Zouari, Crystal structure, optical and electrical properties of metal-halide compound [C7H16N2][ZnCl4], *J. Phys. Chem. Solids*, 2019, **129**, 71–80, DOI: **10.1016/j.jpcs.2018.12.039**.

3 S. Deng, J. Li, X. Chen, Y. Hou and L. Chen, A novel ferroelectric based on quinuclidine derivatives, *Chin. Chem. Lett.*, 2020, **31**, 1686–1689, DOI: **10.1016/j.cclet.2019.11.011**.

4 X.-P. Wang, H.-F. Ni, Q.-F. Luo, G. Teri, J.-Q. Wang, C.-F. Wang, Y. Zhang and D.-W. Fu, Reversible Phase Transition and Dielectric Response of Hybrid Lead-Free Antimony-Based Crystals, *Crys. Growth Des.*, 2024, **24**, 4728–4735, DOI: **10.1021/acs.cgd.4c00323**.

5 Y.-Y. Tang, P.-F. Li, P.-P. Shi, W.-Y. Zhang, Z.-X. Wang, Y.-M. You, H.-Y. Ye, T. Nakamura and R.-G. Xiong, Visualization of Room-Temperature Ferroelectricity and Polarization Rotation in the Thin Film of Quinuclidinium Perrhenate, *Phys. Rev. Lett.*, 2017, **119**, 207602, DOI: **10.1103/PhysRevLett.119.207602**.

6 I. Be, H. Sadok, F. Hajlaoui, K. Karoui, N. Audebrand, T. Roisnel and N. Zouari, Crystal structure, phase transitions, optical and electrical properties in a new Cu-halide organic-inorganic hybrid, *J. Mol. Struct.*, 2019, **1186**, 118–126, DOI: **10.1016/j.molstruc.2019.03.025**.

7 C.-Y. Yue, N. Lin, L. Gao, Y.-X. Jin, Z.-Y. Liu, Y.-Y. Cao, S.-S. Han, X.-K. Lian, B. Hu and X.-W. Lei, Organic cation directed one-dimensional cuprous halide compounds: syntheses, crystal structures and photoluminescence properties, *Dalton Trans.*, 2019, **48**, 10151–10159, DOI: **10.1039/C9DT01460H**.

8 W. Xiao, X. Wang, R. Liu and J. Wu, Quinuclidine and its derivatives as hydrogen-atom-transfer catalysts in photoinduced reactions, *Chin. Chem. Lett.*, 2021, **32**, 1847–1856, DOI: **10.1016/j.cclet.2021.02.009**.

9 A. R. Fernandes, E. Sanchez-Lopez, A. Santini, T. D. Santos, M. L. Garcia, A. M. Silva and E. B. Souto, Mono- and Dicationic DABCO/Quinuclidine Composed Nanomaterials for the Loading of Steroidal Drug: 32 Factorial Design and Physicochemical Characterization, *Nanomaterials*, 2021, **11**(10), 2758, DOI: **10.3390/nano11102758**.

10 A. Cizman, D. A. Kowalska, M. Trzebiatowska, W. Medycki, M. Krupiński, P. Staniorowski and R. Poprawski, The structure and switchable dielectric properties of a dabco complex with chromium chloride, *Dalton Trans.*, 2020, **49**, 10394–10401, DOI: **10.1039/D0DT01897J**.

11 E. Jach, D. A. Kowalska, M. A. Gusowski, M. Trzebiatowska, M. Krupinski, W. Medycki, J. Jędryka, P. Staniorowski and A. Ciżman, Dynamics of Organic Cations in Switchable Quinuclidinium Metal Chloride Dielectrics, *J. Phys. Chem. C*, 2023, **127**(5), 2589–2602, DOI: **10.1021/acs.jpcc.2c07218**.

12 A. Sen, S. Roy, S. C. Peter, A. Paul, U. V. Waghmare and A. Sundaresan, Order-disorder structural phase transition and magnetocaloric effect in organic-inorganic halide hybrid (C2H5NH3)2CoCl4, *J. Solid State Chem.*, 2018, **258**, 431–440, DOI: **10.1016/j.jssc.2017.10.036**.

13 D. P. Panda, D. Swain and A. Sundaresan, Photophysical and Magnetic Properties in Zero-Dimensional (H2DABCO) MX4·nH$_2$O (M = Mn and Cu; X = Cl and Br; n = 0, 1, and 4), *J. Phys. Chem. C*, 2022, **126**(31), 13291–13299, DOI: **10.1021/acs.jpcc.2c03481**.

14 S. Maderlehner, M. J. Leitl, H. Yersin and A. Pfitzner, Halocuprate(I) zigzag chain structures with *N*-methylated DABCO cations – bright metal-centered luminescence and thermally activated color shifts, *Dalton Trans.*, 2015, **44**, 19305–19313, DOI: **10.1039/C5DT02709H**.

15 N. Hoshino and T. Akutagawa, Inversion Symmetry Breaking in Order–Disorder Transitions of Globular Ligands Coordinating to Cobalt(II) and Nickel(II) Bisacetylacetonato Complexes During Heating, *Chem. Eur. J.*, 2021, **27**(12), 4064–4069, DOI: **10.1002/chem.202004492**.

16 E. Jach, D. A. Kowalska, M. Trzebiatiowska, W. Medycki, A. Ostrowski, W. Bednarski, M. Gusowski, P. Staniorowski, A. Bartoszewicz, U. Diu and A. Ciżman, Structural Diversity and Stability of Organic–Inorganic Hybrid Quinuclidine-Based Metal Bromides, *Inorg. Chem.*, 2025, **64**(15), 7422–7436, DOI: **10.1021/acs.inorgchem.5c00039**.

17 P.-F. Li, Y.-Y. Tang, Z.-X. Wang, H. Y. Ye, Y.-M. You and R.-G. Xieong, Anomalously rotary polarization discovered in homochiral organic ferroelectrics, *Nat. Commun.*, 2016, **7**, 13635, DOI: **10.1038/ncomms13635**.

18 J. Lee, W. Seol, G. Anoop, S. Samanta, S. Unithrattil, D. Ahn, W. Kim, G. Jung and J. Jo, Stabilization of Ferroelectric Phase in Highly Oriented Quinuclidinium Perrhenate (HQReO$_4$) Thin Films, *Materials*, 2021, **14**, 2126, DOI: **10.3390/ma14092126**.

19 Rigaku Oxford Diffraction, *CrysAlisPro Software System, Version 1.171*, Rigaku Corporation, Oxford, U.K., 2020.

20 G. M. Sheldrick, SHELXT – Integrated space-group and crystalstructure determination, *Acta Crystallogr., Sect. A: Found. Adv.*, 2015, **71**, 3–8.

21 G. M. Sheldrick, Crystal structure refinement with SHELXL, *Acta Crystallogr., Sect. C:Struct. Chem.*, 2015, **71**, 3–8.

22 O. V. Dolomanov, L. J. Bourhis, R. J. Gildea, J. A. K. Howard and H. Puschmann, OLEX2 A Complete Structure Solution, Refinement and Analysis Program, *J. Appl. Crystallogr.*, 2009, **42**, 339–341.

23 S. Grimme, Semiempirical GGA-type density functional constructed with a long-range dispersion correction, *J. Comput. Chem.*, 2006, **27**, 1787, DOI: **10.1002/jcc.20495**.

24 Y. Zhao and D. G. Truhlar, The M06 suite of density functionals for main group thermochemistry, thermochemical kinetics, noncovalent interactions, excited states, and transition elements: two new functionals and systematic testing of four M06-class functionals and 12 other func-

tionals, *Theor. Chem. Acc.*, 2008, **120**, 215–241, DOI: 10.1007/s00214-007-0310-x.

25 Y. Zhao and D. G. Truhlar, A new local density functional for main-group thermochemistry, transition metal bonding, thermochemical kinetics, and noncovalent interactions, *J. Chem. Phys.*, 2006, **125**, 194101, DOI: 10.1063/1.2370993.

26 J. M. Tao, J. P. Perdew, V. N. Staroverov and G. E. Scuseria, Climbing the density functional ladder: Nonempirical meta-generalized gradient approximation designed for molecules and solids, *Phys. Rev. Lett.*, 2003, **91**, 146401, DOI: 10.1103/PhysRevLett.91.146401.

27 H. Iikura, T. Tsuneda, T. Yanai and K. Hirao, Long-range correction scheme for generalized-gradient-approximation exchange functionals, *J. Chem. Phys.*, 2001, **115**, 3540–3544, DOI: 10.1063/1.1383587.

28 A. C. Neto and F. E. Jorge, All-electron double zeta basis sets for the most fifth-row atoms: Application in DFT spectroscopic constant calculations, *Chem. Phys. Lett.*, 2013, **582**, 158–162, DOI: 10.1016/j.cplett.2013.07.045.

29 A. Z. Oliveira, I. B. Ferreira, C. T. Campos, F. E. Jorge and P. A. Fantin, Segmented all-electron basis sets of triple zeta quality for the lanthanides: application to structure calculations of lanthanide monoxides, *J. Mol. Model.*, 2019, **25**, 38, DOI: 10.1007/s00894-019-3924-8.

30 F. N. N. Pansini, A. C. Neto, M. de Campos and R. M. de Aquino, Effects of All-Electron Basis Sets and the Scalar Relativistic Corrections in the Structure and Electronic Properties of Niobium Clusters, *J. Phys. Chem. A*, 2017, **121**, 5728–5734, DOI: 10.1021/acs.jpca.7b04600.

31 M. L. Neto, K. L. Agra, J. S. Filho and F. E. Jorge, TDDFT calculations and photoacoustic spectroscopy experiments used to identify phenolic acid functional biomolecules in Brazilian tropical fruits in natura, *Spectrochim. Acta, Part A*, 2018, **193**, 249–257, DOI: 10.1016/j.saa.2017.12.036.

32 M. J. Frisch, G. W. Trucks, H. B. Schlegel, G. E. Scuseria, M. A. Robb, J. R. Cheeseman, G. Scalmani, V. Barone, G. A. Petersson, H. Nakatsuji, X. Li, M. Caricato, A. V. Marenich, J. Bloino, B. G. Janesko, R. Gomperts, B. Mennucci, H. P. Hratchian, J. V. Ortiz, A. F. Izmaylov, J. L. Sonnenberg, D. Williams-Young, F. Ding, F. Lipparini, F. Egidi, J. Goings, B. Peng, A. Petrone, T. Henderson, D. Ranasinghe, V. G. Zakrzewski, J. Gao, N. Rega, G. Zheng, W. Liang, M. Hada, M. Ehara, K. Toyota, R. Fukuda, J. Hasegawa, M. Ishida, T. Nakajima, Y. Honda, O. Kitao, H. Nakai, T. Vreven, K. Throssell, J. A. Montgomery Jr., J. E. Peralta, F. Ogliaro, M. J. Bearpark, J. J. Heyd, E. N. Brothers, K. N. Kudin, V. N. Staroverov, T. A. Keith, R. Kobayashi, J. Normand, K. Raghavachari, A. P. Rendell, J. C. Burant, S. S. Iyengar, J. Tomasi, M. Cossi, J. M. Millam, M. Klene, C. Adamo, R. Cammi, J. W. Ochterski, R. L. Martin, K. Morokuma, O. Farkas, J. B. Foresman and D. J. Fox, *Gaussian 16, Revision A.03*, Gaussian, Inc., Wallingford CT, 2016.

33 K. Momma and F. Izumi, *VESTA* 3 for three-dimensional visualization of crystal, volumetric and morphology data, *J. Appl. Crystallogr.*, 2011, **44**(6), 1272–1276, DOI: 10.1107/S0021889811038970.

34 D. Rosiak, A. Okuniewski and J. Chojnacki, Novel complexes possessing Hg-(Cl, Br, I)⋯O=C halogen bonding and unusual Hg2S2(Br/I)4 kernel. The usefulness of τ4′ structural parameter, *Polyhedron*, 2018, **146**, 35–41, DOI: 10.1016/j.poly.2018.02.016.

35 H.-L. Cai, W. Zhang, J.-Z. Ge, Y. Zhang, K. Awaga, T. Nakamura and R.-G. Xiong, 4-(cyanomethyl)anilinium Perchlorate: A New Displacive-Type Molecular Ferroelectric, *Phys. Rev. Lett.*, 2011, **107**, 147601–114766, DOI: 10.1103/PhysRevLett.107.147601.

36 Z.-S. Yao, K. Yamamoto, H. L. Cai, K. Akahashi and O. Sato, Above Room Temperature Organic Ferroelectrics: Diprotonated 1,4-Diazabicyclo[2.2.2]octane Shifts between Two 2-Chlorobenzoates, *J. Am. Chem. Soc.*, 2016, **138**(37), 12005–12008, DOI: 10.1021/jacs.6b03747.

37 H. Seggern and S. N. Fedosov, Conductivity induced polarization in two-phase ferroelectric materials, Proceedings. 11th International Symposium on Electrets, Melbourne, VIC, Australia, 2002, 211–214, DOI:DOI: 10.1109/ISE.2002.1042981.

38 N. Wei, D. Zhand, F. Yand, X. Han, Z. Zhong and K. Zeng, Effect of electrical conductivity on the polarization behaviour and pyroelectric, piezoelectric property prediction of 0–3 ferroelectric composites, *J. Phys. D: Appl. Phys.*, 2007, **40**, 2716, DOI: 10.1088/0022-3727/40/9/006.

39 M. Wada, M. Suzuki, A. Sawada, Y. Ishibashi and K. Gesi, Ferroelectricity in $[N(CH_3)_4]_2CuBr_4$ Crystal, *J. Phys. Soc. Jpn.*, 1981, **50**(6), 1813–1814, DOI: 10.1143/JPSJ.50.1813.

40 W. Zhang, H.-Y. Ye, H.-L. Cai, J.-Z. Ge, R.-G. Xiong and S. D. Huang, Discovery of New Ferroelectrics: $[H_2dbco]_2\cdot[Cl_3]\cdot[CuCl_3(H_2O)_2]\cdot H_2O$ (dbco = 1,4-Diaza-bicyclo[2.2.2]octane), *J. Am. Chem. Soc.*, 2010, **132**(21), 7300–7302, DOI: 10.1021/ja102573h.

41 H. Y. Ye, Y. Zhang, S. Noro, K. Kubo, M. Yoshitake, Z. Q. Liu, H. L. Cai, D. W. Fu, H. Yoshikawa, K. Awaga, R. G. Xiong and T. Nakamura, Molecule-displacive ferroelectricity in organic supramolecular solids, *Sci. Rep.*, 2013, **3**, 2249, DOI: 10.1038/srep02249.

42 L. Y. Sheng, D. C. Han, R. K. Huang, L. M. Cao, C. T. He, Z. Y. Du and T. Nakamura, Tadpole-Like Polar Molecule Encapsulated in a Two-in-One Supramolecular Cage: Molecular Motion, Phase Transition and Ferroelectricity, *J. Am. Chem. Soc.*, 2024, **146**(33), 22893–22898, DOI: 10.1021/jacs.4c06859.

43 F. Jona and G. Shirane, *Ferroelectric Crystals*, Pergamon, 1962.

44 K. Ding, H. Ye, C. Su, Y.-A. Xiong, G. Du, Y.-M. You, Z. X. Zhang, S. Dong, Y. Zhang and D. W. Fu, Superior ferroelectricity and nonlinear optical response in a hybrid germanium iodide hexagonal perovskite, *Nat. Commun.*, 2023, **14**, 2863, DOI: 10.1038/s41467-023-38590-7.

45 B. Rhaiem, S. Chouaib and K. Guidara, Dielectric relaxation and ionic conductivity studies of Ag2ZnP2O7, *Ionic*, 2010, **16**, 455–463, DOI: 10.1007/s11581-009-0411-8.

46 N. Salah, B. Hamdi, N. Bouzidia and A. B. Salah, Crystal Structures, Hirshfeld Surface Analysis, Thermal Behavior and Dielectric Properties of a New Organic-Inorganic Hybrid [C6H10(NH3)2]Cu2Cl8, *J. Mol. Struct.*, 2017, 414–425, DOI: **10.1016/j.molstruc.2017.08.002**.

47 M. Belhaj Salah, N. Nouiri, K. Jaouadi, T. Mhiri and N. Zouari, Synthesis, crystal structure, thermal analysis and dielectric properties of $Rb_4(SO_4)(HSO_4)_2(H_3AsO_4)$ compound, *J. Mol. Struct.*, 2018, **1151**, 286–300, DOI: **10.1016/j.molstruc.2017.09.025**.

48 N. Salah, B. Hamdi and A. B. Salah, Synthesis, Crystal Structure, Thermal and Dielectric Properties and Optical Band Gap Study of the Organic–Inorganic Hybrid Compound $[H(C_{10}H_{10}N_2)]_4Cu_4Cl_8$, *J. Cluster Sci.*, 2016, **27**, 1777–1795, DOI: **10.1007/s10876-016-1039-2**.

49 S. Zaghden, H. B. Attia, M. S. M. Abdelbaky, A. Oueslati, S. García-Granda, M. Dammak and L. Ktari, Characterization of a New Hybrid Compound (C3H8N6) 2ZnCl4·2Cl: X-ray Structure, Hirshfeld Surface, Vibrational, Thermal Stability, Dielectric Relaxation, and Electrical Conductivity, *ACS Omega*, 2024, **9**, 47597–47612, DOI: **10.1021/acsomega.4c06685**.

50 K. Kahouli, A. B. J. Kharrat, K. Khirouni and S. Chaabouni, Electrical conduction mechanism and dielectric properties of the $[C_{13}H_{16}N_2]_5(BiCl_6)_3Cl$ hybrid compound, *Appl. Phys. A*, 2023, **129**, 431, DOI: **10.1007/s00339-023-06697-9**.

51 J. B. Jorcin, M. E. Orazem, N. Pebere and B. Tribollet, Determination of effective capacitance and film thickness from constant-phase-element parameters, *Electrochim. Acta*, 2006, **51**, 1473–1479, DOI: **10.1016/j.electacta.2009.10.065**.

52 B. Hirschorn, M. E. Orazem, B. Tribollet, V. Vivier, I. Frateur and M. Musiani, Determination of effective capacitance and film thickness from constant-phase-element parameters, *Electrochim. Acta*, 2010, **55**, 6218–6227, DOI: **10.1016/j.electacta.2009.10.065**.

53 S. Miga, J. Dec and W. Kleem, Non-Linear Dielectric Response of Ferroelectrics, Relaxors and Dipolar Glasses, in *Ferroelectrics - Characterization and Modeling*, InTech, 2011, pp. 181–181. DOI: **10.5772/20380**.

54 C. Ang and Z. Yu, Dc Electric-Field Dependence of the Dielectric Constant in Polar Dielectrics: Multipolarization Mechanism Model, *Phys. Rev. B:Condens. Matter Mater. Phys.*, 2004, **69**(17), 174109, DOI: **10.1103/PhysRevB.69.174109**.

55 L. N. Patro, O. Burghaus and B. Roling, Nonlinear Ion Transport in the Supercooled Ionic Liquid 1-Hexyl-3-Methylimidazolium Bis(Trifluoromethylsulfonyl)Imide: Frequency Dependence of Third-Order and Fifth-Order Conductivity Coefficients, *J. Chem. Phys.*, 2015, **142**, 064505, DOI: **10.1063/1.4907373**.

56 H. Staesche and B. Roling, Nonlinear Conductivity Spectra of Ionically Conducting Glasses and Glass Ceramics: Analysis of Spectral Shape and Scaling Properties, *Phys. Rev. B:Condens. Matter Mater. Phys.*, 2010, **82**(13), 134202, DOI: **10.1103/PhysRevB.82.134202**.

57 N. A. Wojcik, P. Kupracz and R. J. Baczynski, Nonlinear electrical properties of glass-ceramics nanocomposites containing ferroelectric nanocrystallites of $Bi_2VO_{5.5}$, *Solid State Ionics*, 2018, **317**, 7–14, DOI: **10.1016/j.ssi.2017.12.035**.

58 C. J. F. Böttcher, Theory of Electric Polarization, in *Dielectric in static fields*, Elsevier, 1973, DOI: **10.1016/C2009-0-15579-4**.

59 H. Staeche, S. Murugavel and B. Roling, Nonlinear Conductivity and PermittivitySpectra of Ion Conducting GlassesZ, *Phys. Chem.*, 2009, **223**, 1229–1238, DOI: **10.1524.zpch.2009.607**.

60 L. N. O. Patro and O. B. Burhgaus, Nonlinear ion transport in the supercooled ionic liquid 1-hexyl-3-methylimidazolium bis(trifluoromethylsulfonyl)imide: Frequency dependence of third-order and fifth-order conductivity coefficients, *J. Chem. Phys.*, 2015, **142**, 064505, DOI: **10.1063/1.4907373**.

61 M. Trzebiatowska, D. A. Kowalska, A. Ciżman, N. A. Wójcik, R. J. Barczyński, A. Pikul, J. K. Zaręba, M. Palewicz, T. Piasecki, K. Roleder, M. Gusowski and M. Mączka, The influence of azide and imidazole on the properties of Mn- and Cd-based networks: conductivity and nonlinear phenomena, *J. Mater. Chem. C*, 2024, **12**, 15119–15136, DOI: **10.1039/D4TC02745K**.

62 R. W. Boyd, Order-of-magnitude estimates of the nonlinear optical susceptibility, *J. Mod. Opt.*, 1999, **46**(3), 367–378, DOI: **10.1080/09500349908231277**.

63 (*a*) CCDC 2417202: Experimental Crystal Structure Determination, 2025, DOI: **10.5517/ccdc.csd.cc2m498c**; (*b*) CCDC 2417203: Experimental Crystal Structure Determination, 2025, DOI: **10.5517/ccdc.csd.cc2m499d**.